

# The MARTINI Force Field: Coarse Grained Model for Biomolecular Simulations

Siewert J. Marrink,<sup>\*,†</sup> H. Jelger Risselada,<sup>†</sup> Serge Yefimov,<sup>‡</sup> D. Peter Tieleman,<sup>§</sup> and Alex H. de Vries<sup>†</sup>

Groningen Biomolecular Sciences and Biotechnology Institute & Zernike Institute for Advanced Materials, Department of Biophysical Chemistry, University of Groningen, Nijenborgh 4, 9747 AG Groningen, The Netherlands, Zernike Institute for Advanced Materials, Department of Applied Physics, University of Groningen, Nijenborgh 4, 9747 AG Groningen, The Netherlands, and Department of Biological Sciences, University of Calgary, 2500 University Drive NW, Calgary AB T2N 1N4, Canada

Received: February 8, 2007; In Final Form: April 25, 2007

We present an improved and extended version of our coarse grained lipid model. The new version, coined the MARTINI force field, is parametrized in a systematic way, based on the reproduction of partitioning free energies between polar and apolar phases of a large number of chemical compounds. To reproduce the free energies of these chemical building blocks, the number of possible interaction levels of the coarse-grained sites has increased compared to those of the previous model. Application of the new model to lipid bilayers shows an improved behavior in terms of the stress profile across the bilayer and the tendency to form pores. An extension of the force field now also allows the simulation of planar (ring) compounds, including sterols. Application to a bilayer/cholesterol system at various concentrations shows the typical cholesterol condensation effect similar to that observed in all atom representations.

## 1. Introduction

The use of coarse grained (CG) models in a variety of simulation techniques has proven to be a valuable tool to probe the time and length scales of systems beyond what is feasible with traditional all atom (AA) models. Applications to lipid systems in particular, pioneered by Smit,<sup>1</sup> have become widely used (for recent reviews see refs 2–4). A large diversity of coarse graining approaches is available; they range from qualitative, solvent-free models (e.g., refs 5–12) via more realistic models with explicit but simplified water (e.g., refs 1 and 13–21) to models including chemical specificity.<sup>22–26</sup> Models within this latter category are typically parametrized based on comparison to atomistic simulations, using inverted Monte Carlo schemes<sup>22,25,26</sup> or force matching<sup>24</sup> approaches. Our own model<sup>23</sup> has also been developed in close connection with more detailed atomistic models; however, the philosophy of our coarse graining approach is different. Instead of focusing on an accurate reproduction of structural details at a particular state point for a specific system, we aim for a broader range of applications without the need to reparametrize the model each time. We do so by extensive calibration of the building blocks of the coarse grained force field against thermodynamic data, in particular oil/water partitioning coefficients. This is similar in spirit to the recent development of the GROMOS force field.<sup>27</sup> Processes such as lipid self-assembly, peptide membrane binding or protein–protein recognition depend critically on the degree to which the constituents partition between polar and nonpolar environments. The use of a consistent strategy for the development of compatible coarse grained and atomic level force fields

is of additional importance for its intended use in multiscale applications.<sup>28–31</sup>

The list of applications of our coarse grained model to date includes vesicle formation and fusion,<sup>32–34</sup> lamellar phase transformations,<sup>35–37</sup> the structure and dynamics of membrane-protein assemblies,<sup>38,39</sup> the structure of bicelles,<sup>40</sup> the equation of state of monolayers,<sup>41,42</sup> and the effect of various molecules on membranes (butanol,<sup>43</sup> DMSO,<sup>44</sup> dendrimers<sup>45</sup>). In most of these studies the CG model, sometimes with small changes from the published version, performed well in comparison either to experimental data or to more detailed atomistic models. A very useful set of simulations was performed by Baron and co-workers<sup>46–48</sup> in which the CG model was systematically compared to AA models. In the first paper of this series<sup>46</sup> the configurational entropies for hydrocarbons were compared. It was found that the CG model provides a good description of the overall chain flexibility and configurations. Furthermore, the acceleration of the sampling of the phase space by the CG model was estimated to be between 5- and 10-fold, a speed-up comparable to the original estimate based on comparison of diffusion rates.<sup>23</sup> Very similar conclusions were drawn from the analysis of chain configurations in lipid bilayers.<sup>47</sup> The absolute entropies of hydrocarbon chains, however, differ considerably in the CG and atomistic simulations, which is a direct effect of the neglect of atomic degrees of freedom in the CG simulations. In the CG model the neglect of this entropy term is (necessarily) compensated for by a reduced enthalpy term. This compensation has been clearly demonstrated in a subsequent comparison study of thermodynamic properties of AA and CG alkanes.<sup>48</sup>

Within the limitations set by the neglect of some degrees of freedom in the CGing procedure, there is room for improvement over the originally published force field.<sup>23</sup> A number of recommendations were given to improve the performance of the CG model based on the comparison between AA and CG simulations of alkanes mentioned before.<sup>46,47</sup> Furthermore,

\* Corresponding author. E-mail: s.j.marrink@rug.nl.

<sup>†</sup> Groningen Biomolecular Sciences and Biotechnology Institute & Zernike Institute for Advanced Materials, Department of Biophysical Chemistry, University of Groningen.

<sup>‡</sup> Zernike Institute for Advanced Materials, Department of Applied Physics, University of Groningen.

<sup>§</sup> Department of Biological Sciences, University of Calgary.

studies of the lamellar to inverted hexagonal phase transformation<sup>35</sup> and of the stability of bicelles<sup>40</sup> suggested that the spontaneous curvature of CG phospholipids is too negative, i.e., the tendency to form nonlamellar aggregates is too high. In both studies an ad hoc solution (increasing the hydration strength of the phosphate moiety) was found to lead to improved behavior. Furthermore, the original CG model uses a water model which has a tendency to freeze too easily, especially in confined geometries (e.g., sandwiched between membranes). Finally, the original model suffers from a somewhat too coarsened definition of interaction energy levels, making the mapping of CG interaction sites to real chemical compounds unnecessarily crude.

Here we present an improved version of the CG forcefield in which we solve the problems mentioned above by (i) including more interaction energy levels and particle types and (ii) performing a thorough analysis of partition free energies linked to chemical functional groups, without compromising the speed and simplicity of the previous version. In addition, we present a protocol that allows the modeling of ring structures, with an application to cholesterol. The new force field is coined the MARTINI force field for biomolecular simulations. For one, Martini is the nickname of the city of Groningen where the force field was developed. It also reflects the universality of the cocktail with the same name; how a few simple ingredients (read: chemical building blocks) can be endlessly varied to create a complex palette of taste. The version described in this paper should be referred to as MARTINI 2.0.

The rest of this paper is organized as follows. A detailed description of the new force field is presented in the next section. The results/discussion section is subdivided into three main parts: first it is shown how partitioning free energies of a large range of small compounds can be reproduced; subsequently the improved behavior for DPPC (dipalmitoyl-phosphatidylcholine) membranes is illustrated; and finally the newly derived parameters for ring structures are applied to a DPPC/cholesterol system.

## 2. Model

**2.1. Interaction Sites.** Similar to the previous model,<sup>23</sup> the updated model is based on a four-to-one mapping, i.e., on average four heavy atoms are represented by a single interaction center. For ring structures a different mapping is introduced, as will be explained below. In order to keep the model simple, we still consider only four main types of interaction sites: polar (P), nonpolar (N), apolar (C), and charged (Q). Each particle type has a number of subtypes, which allow for a more accurate representation of the chemical nature of the underlying atomic structure. Compared to the previous version, the total number of subtypes has increased from 9 to 18. Within a main type, subtypes are either distinguished by a letter denoting the hydrogen-bonding capabilities (d = donor, a = acceptor, da = both, 0 = none), or by a number indicating the degree of polarity (from 1, low polarity, to 5, high polarity). The mapping of some of the molecules studied in this paper is shown in Figure 1. All graphical images presented in this paper were prepared using VMD.<sup>49</sup>

**2.2. Nonbonded Interactions.** The form of the interaction potentials remains unchanged from the previous model. A shifted Lennard-Jones (LJ) 12-6 potential energy function is used to describe the nonbonded interactions

$$U_{\text{LJ}}(r) = 4\epsilon_{ij} \left[ \left( \frac{\sigma_{ij}}{r} \right)^{12} - \left( \frac{\sigma_{ij}}{r} \right)^6 \right] \quad (1)$$

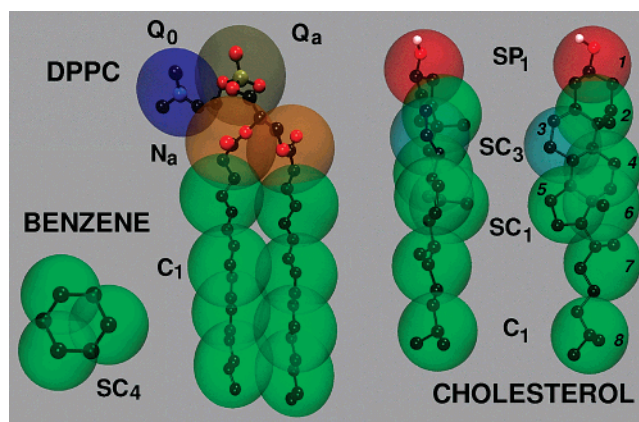


**Figure 1.** Mapping between the chemical structure and the coarse grained model for DPPC, cholesterol, and benzene. The coarse grained bead types which determine their relative hydrophilicity are indicated. The prefix “S” denotes a special class of CG sites introduced to model rings.

with  $\sigma_{ij}$  representing the closest distance of approach between two particles and  $\epsilon_{ij}$  the strength of their interaction. The same effective size,  $\sigma = 0.47$  nm, is assumed for each interaction pair, except for the two special classes of rings and antifreeze particles (see below). There is one other exception: for interactions between charged (Q-type) and the most apolar types (C<sub>1</sub> and C<sub>2</sub>) the range of repulsion is extended by setting  $\sigma = 0.62$  nm. This change makes it more favorable for charged particles to keep their hydration shells when dragged into an apolar medium. The interactions within the new model are now divided into 10 levels, instead of the 5 levels in the previous version. This allows for more fine-tuning in the reproduction of experimental solubilities. The interaction strength  $\epsilon$  of each of the interaction levels is as follows: O,  $\epsilon = 5.6$  kJ/mol; I,  $\epsilon = 5.0$  kJ/mol; II,  $\epsilon = 4.5$  kJ/mol; III,  $\epsilon = 4.0$  kJ/mol; IV,  $\epsilon = 3.5$  kJ/mol; V,  $\epsilon = 3.1$  kJ/mol; VI,  $\epsilon = 2.7$  kJ/mol; VII,  $\epsilon = 2.3$  kJ/mol; VIII,  $\epsilon = 2.0$  kJ/mol; and IX,  $\epsilon = 2.0$  kJ/mol (with  $\sigma = 0.62$  nm). The level of interactions between the different CG sites is summarized in Table 1. The most polar interaction, level O, models compounds that are solid at room temperature. It is also used for the strong hydration shell of charged groups. The level I interaction models strong polar interactions as in bulk water, levels II and III model more volatile liquids such as ethanol or acetone, level IV models the nonpolar interactions in aliphatic chains, and levels V–VIII are used to mimic various degrees of hydrophobic repulsion between polar and nonpolar phases. Level IX finally describes the interaction between charged particles and a very apolar medium. Level I corresponds to level I in the previous version of the model, levels II and III are split from the old level II, level IV corresponds to the old level III, level VI to the old level IV, and level VIII to the old level V.

In addition to the LJ interaction, charged groups (type Q) bear a full charge  $q_{i,j}$  interacting via a shifted Coulombic potential energy function

$$U_{\text{el}}(r) = \frac{q_i q_j}{4\pi\epsilon_0\epsilon_r r} \quad (2)$$

with relative dielectric constant  $\epsilon_r = 15$  for explicit screening. The strength of the screening has been reduced slightly (from  $\epsilon_r = 20$ ) with respect to the previous version of the model. This change was required to balance the increased hydration strength of many of the CG particle types in comparison to the previous model. In combination with a decreased screening, key structural

**TABLE 1: Interaction Matrix<sup>a</sup>**

	sub	Q				P					N				C				
		da	d	a	0	5	4	3	2	1	da	d	a	0	5	4	3	2	1
Q	da	O	O	O	II	O	O	O	I	I	I	I	I	IV	V	VI	VII	IX	IX
	d	O	I	O	II	O	O	O	I	I	I	III	I	IV	V	VI	VII	IX	IX
	a	O	O	I	II	O	O	O	I	I	I	I	III	IV	V	VI	VII	IX	IX
	0	II	II	II	IV	I	O	I	II	III	III	III	III	IV	V	VI	VII	IX	IX
P	5	O	O	O	I	O	O	O	O	O	I	I	I	IV	V	VI	VI	VII	VIII
	4	O	O	O	O	O	I	I	II	II	III	III	III	IV	V	VI	VI	VII	VIII
	3	O	O	O	I	O	I	I	II	II	II	II	II	IV	IV	V	V	VI	VII
	2	I	I	I	II	O	II	II	II	II	II	II	II	III	IV	IV	V	VI	VII
N	1	I	I	I	III	O	II	II	II	II	II	II	II	III	IV	IV	IV	V	VI
	da	I	I	I	III	I	III	II	II	II	II	II	II	IV	IV	V	VI	VI	VI
	d	I	III	I	III	I	III	II	II	II	II	III	II	IV	IV	V	VI	VI	VI
	a	I	I	III	III	I	III	II	II	II	II	II	III	IV	IV	V	VI	VI	VI
C	0	IV	IV	IV	IV	IV	IV	IV	III	III	IV	IV	IV	IV	IV	IV	IV	V	VI
	5	V	V	V	V	V	V	IV	IV	IV	IV	IV	IV	IV	IV	IV	IV	V	V
	4	VI	VI	VI	VI	VI	VI	V	IV	IV	V	V	V	IV	IV	IV	IV	V	V
	3	VII	VII	VII	VII	VI	VI	V	V	IV	VI	VI	VI	IV	IV	IV	IV	IV	IV
	2	IX	IX	IX	IX	VII	VII	VI	VI	V	VI	VI	VI	V	V	V	IV	IV	IV
	1	IX	IX	IX	IX	VIII	VIII	VII	VII	VI	VI	VI	VI	VI	V	V	IV	IV	IV

<sup>a</sup> Level of interaction indicates the well depth in the LJ potential: O,  $\epsilon = 5.6$  kJ/mol; I,  $\epsilon = 5.0$  kJ/mol; II,  $\epsilon = 4.5$  kJ/mol; III,  $\epsilon = 4.0$  kJ/mol; IV,  $\epsilon = 3.5$  kJ/mol; V,  $\epsilon = 3.1$  kJ/mol; VI,  $\epsilon = 2.7$  kJ/mol; VII,  $\epsilon = 2.3$  kJ/mol; VIII,  $\epsilon = 2.0$  kJ/mol; IX,  $\epsilon = 2.0$  kJ/mol. The LJ parameter  $\sigma = 0.47$  nm for all interaction levels except level IX for which  $\sigma = 0.62$  nm. Four different CG sites are considered: charged (Q), polar (P), nonpolar (N), and apolar (C). Subscripts are used to further distinguish groups with different chemical nature: 0, no hydrogen-bonding capabilities are present; d, groups acting as hydrogen bond donor; a, groups acting as hydrogen bond acceptor; da, groups with both donor and acceptor options; 1–5, indicating increasing polar affinity.

properties such as the area per lipid for many different lipid types or the coordination number of ions in solution could be maintained at the same level of accuracy as obtained with the previous parametrization.<sup>23</sup>

**2.3. Bonded Interactions.** Bonded interactions between chemically connected sites are kept unaltered with respect to the previous version of the model. Bonds are described by a weak harmonic potential  $V_{\text{bond}}(R)$

$$V_{\text{bond}}(R) = \frac{1}{2} K_{\text{bond}} (R - R_{\text{bond}})^2 \quad (3)$$

with an equilibrium distance  $R_{\text{bond}} = \sigma = 0.47$  nm and a force constant of  $K_{\text{bond}} = 1250$  kJ mol<sup>-1</sup> nm<sup>-2</sup>. The LJ interaction is excluded between bonded particles. Bonded particles, on average, are somewhat closer to each other than neighboring nonbonded particles (for which the equilibrium distance is  $2^{1/6}\sigma$ ). The use of a single equilibrium bond distance and force constant is not a prerequisite, however. Different values may be used to better reflect the underlying chemical structure. To represent chain stiffness, a weak harmonic potential  $V_{\text{angle}}(\theta)$  of the cosine type is used for the angles

$$V_{\text{angle}}(\theta) = \frac{1}{2} K_{\text{angle}} \{\cos(\theta) - \cos(\theta_0)\}^2 \quad (4)$$

LJ interactions between second nearest neighbors are not excluded. For aliphatic chains, the force constant remains at  $K_{\text{angle}} = 25$  kJ mol<sup>-1</sup> with an equilibrium bond angle  $\theta_0 = 180^\circ$ . Extensive analysis<sup>46</sup> of the angle distributions and configurational entropy of aliphatic chains modeled with our previous coarse grained model compared to an atomistic model has revealed that the CG model performs very well. For cis-unsaturated bonds, the same study showed that the force constant was slightly too weak to reproduce the mapped angle distribution obtained from the atomistic simulation. Therefore, in the new model, the force constant for the angles involving the cis double bond is set to  $K_{\text{angle}} = 45$  kJ mol<sup>-1</sup> (the original value  $K_{\text{angle}} = 35$  kJ mol<sup>-1</sup>). The equilibrium angle remains at  $\theta_0 = 120^\circ$ . Using the same approach for trans-unsaturated bonds, we obtain

the best fit to atomistic models with an equal force constant  $K_{\text{angle}} = 45$  kJ mol<sup>-1</sup> and  $\theta_0 = 180^\circ$ .

**2.4. Ring Particles.** In order to preserve the geometry of small ring compounds, a four-to-one mapping procedure is inadequate. The strategy to model rings is therefore to include as many CG sites as necessary in order to keep the ring geometry, typically resulting in a 2 or 3 to 1 mapping of ring atoms onto CG beads. With this more detailed mapping, enough geometrical detail is kept to mimic the geometry of small compounds such as cyclohexane or benzene and sterol bodies such as cholesterol (see Figure 1). As a consequence of the large density of CG beads, the interaction parameters for ring particles need special treatment. In the new model, we introduce a special particle set, labeled “S”, which can be used to model ring structures. In this set, the effective interaction size and strength for ring–ring interactions is reduced compared to the normal set. Specifically, the  $\sigma$  of the LJ potential is set to 0.43 rather than 0.47 nm and the  $\epsilon$  is scaled to 75% of the original value. This allows ring particles to pack more closely together without freezing, which allows reproduction of the liquid densities of small ring compounds while retaining the correct partitioning behavior. Thus, a hydrophobic particle of type SC<sub>1</sub> (C<sub>1</sub> of set S), being part of a cyclohexane ring, will interact with like particles using a LJ potential with  $\epsilon = 0.75 \times 3.5$  kJ mol<sup>-1</sup> and  $\sigma = 0.43$  nm. Its interaction with C<sub>1</sub> particles of normal type will be unaffected, i.e.,  $\epsilon = 3.5$  kJ mol<sup>-1</sup> and  $\sigma = 0.47$  nm.

Apart from a modification of the effective interaction volume, for ringlike structures equilibrium bond lengths and equilibrium angles are chosen to reflect the underlying geometry as accurately as possible. To preserve the rigidity of the rings, and to avoid fast oscillations arising from very high force constants, bonds or angles can also be replaced by an appropriate set of constraints. Intermolecular LJ interactions are excluded within the ring systems. Furthermore an improper dihedral angle potential can be used for more complicated geometries to prevent out of plane distortions

$$V_{\text{id}}(\theta) = K_{\text{id}} (\theta - \theta_{\text{id}})^2 \quad (5)$$



Here  $\theta$  denotes the angle between the planes constituted between atoms  $i,j,k$  and  $j,k,l$ , with equilibrium angle  $\theta_{\text{id}}$  and force constant  $K_{\text{id}}$ .

**2.5. Antifreeze Particles.** A specific problem of the CG model is that water, modeled as  $P_4$  particles, has a freezing temperature that is somewhat too high compared to real water. Depending on the simulation conditions, the CG water freezes between 280 and 300 K. The freezing process is nucleation driven and therefore stochastic in nature. In practice this means that the CG water can remain fluid for very long times (microseconds, or as long as the simulation is performed). Once a nucleation site has formed, however, the transition to the frozen state is rapid and irreversible. Apart from simulations performed at lower temperatures, rapid freezing is especially a problem in systems where a nucleation site is already present (a solid surface, but even a bilayer surface may act as one) or when periodicity enhances the long range ordering (e.g., for small volumes of water).

In order to prevent this unwanted freezing of the CG water, one could introduce stochastic forces. A more effective practical solution is to add an antifreeze agent, similar to what is done in experimental setups performed at temperatures below the freezing point of water. We introduce so-called antifreeze particles, which interact as a special particle type denoted  $BP_4$  (Big  $P_4$ ). In order to disturb the lattice packing of the uniformly sized solvent particles, the LJ parameter  $\sigma$  for  $BP_4$ – $P_4$  interactions is scaled up to 0.57 nm instead of 0.47 nm. To avoid phase separating of antifreeze and solvent particles, the strength of the  $BP_4$ – $P_4$  interaction is raised to level “O”. The interactions of the  $BP_4$  with any other type of particle, including the self-interaction, remain the same as for normal CG water. If only a small amount (a mole fraction  $n_{\text{AF}} = 0.1$  appears to work effectively) of the normal water beads is replaced by the antifreeze particles, the formation of nucleation sites is prevented and freezing is not observed unless the temperature is lowered to well below the freezing temperature of real water. For instance, freezing of a pure water system with  $n_{\text{AF}} = 0.1$  occurs below 250 K. Mixing of antifreeze particles into the water phase does affect the equilibrium properties of the solvent slightly. Due to their larger size and stronger interaction with other water molecules, addition of antifreeze particles lowers both the density and the self-diffusion constant by about 10% at  $n_{\text{AF}} = 0.1$ . To test whether the introduction of antifreeze particles has an effect on bilayer properties, we simulated a small DPPC bilayer system (128 DPPC lipids, 1500 CG water at  $n_{\text{AF}} = 0.1$ ) and found no effect on any of a number of key properties tested: the area per lipid, the transition temperature for formation of the gel phase, and the lateral self-diffusion constant of lipid molecules did not show any significant change.

**2.6. Simulation Parameters.** The simulations described in this paper were performed with the GROMACS simulation package version 3.0.<sup>50</sup> The parameters and example input files of the applications described in this paper are available at <http://md.chem.rug.nl/~marrink/coarsegrain.html>. It is important to realize that the simulation parameters are part of the force field and cannot be changed without affecting other properties. In the simulations the nonbonded interactions are cut off at a distance  $r_{\text{cut}} = 1.2$  nm. To avoid generation of unwanted noise, the standard shift function of GROMACS<sup>50</sup> is used in which both the energy and force vanish at the cutoff distance. The full expressions for the shifted force can be found in ref 47. The LJ potential is shifted from  $r_{\text{shift}} = 0.9$  nm to  $r_{\text{cut}}$ . The electrostatic potential is shifted from  $r_{\text{shift}} = 0.0$  nm to  $r_{\text{cut}}$ . Shifting of the electrostatic potential in this manner mimics the

effect of a distance-dependent screening. Due to the use of shifted potentials, the neighbor list can be updated every 10 steps using a neighbor list cutoff equal to  $r_{\text{cut}}$ . Using this setup, most systems can be simulated with an integration time step of  $dt = 40$  fs (expressed as actual simulation time), although sometimes a smaller time step is required for stability (25–30 fs). Ring systems presented in this paper were run with  $dt = 30$  fs. Although most properties of CG systems (e.g., densities, potential energies) do not depend on the value of the time step used (differences <1%), the free energy differences are more sensitive. For instance, the values reported in Table 3 are found to shift toward the entropically favored direction, i.e., toward mixing. The free energy differences vary up to ~5% upon a decrease of the time step from 40 to 5 fs. Apparently the larger time step results in a less accurate integration of the equations of motion. However, considering the inherent approximative nature of the underlying CG potentials, this is not problematic per se as long as the time step used in simulations does not differ too much from the time step used for the parametrization.

**2.7. Interpretation of Time Scale.** In general, the interpretation of the time scale in CG simulations is not straightforward. In comparison to atomistic models, the dynamics observed with CG models is faster. The main reason is that the underlying energy landscape is much smoother as a result of the larger particle sizes. The friction arising from the atomic degrees of freedom is simply missing. On the basis of comparison of diffusion constants in CG and atomistically modeled systems, the effective time sampled using our CG model was found to be 2- to 10-fold larger. When interpreting the simulation results with the CG model, one can to a first approximation simply scale the time axis. Somewhat surprisingly, a similar scaling factor appears to describe the general dynamics present in a variety of systems quite well. For instance, water permeation rates across a DPPC membrane and lipid lateral diffusion rates are observed to be in good agreement with experimental measurements after scaling the rates by a factor of 4.<sup>23</sup> More global events, such as the aggregation of lipids into vesicles, also occur on a time scale comparable to atomistic simulations after 4-fold scaling.<sup>51</sup> Likewise, sampling of the configurational space of liquid hydrocarbons and of the lipid tails inside a bilayer was 5- to 10-fold faster for the CG model in comparison to an atomistic model<sup>46,47</sup> if no scaling factor was applied. The simulation times reported in the remainder of the paper are effective times, unless explicitly stated (denoted as simulation time). The standard conversion factor we use is a factor of 4, which is the speed up factor in the diffusional dynamics of CG water compared to real water.<sup>23</sup> Note that the dynamics of the system is affected by the assignment of masses to the CG beads. For reasons of computational efficiency, standard masses  $m = 72$  amu (corresponding to four water molecules) are typically used. Especially for ring systems, however, assignment of standard masses to all sites will lead to significantly underestimated dynamics. For accurate analysis of kinetic properties, more realistic masses should be used in the simulations. However, in homogeneous systems scaling of the kinetic properties based on mass differences can be performed afterward.

**2.8. Topologies. 2.8.1. Solvents.** Four water molecules are represented as a single type  $P_4$  CG site. Dodecane and hexadecane are modeled as a linear chain of three and four  $C_1$  particles, respectively, octanol as a  $C_1$ – $P_1$  combination, chloroform as a  $C_4$  particle, and ether as an  $N_0$  particle. Cyclohexane is modeled by three  $SC_1$  particles in a triangular configuration. The  $SC_1$ – $SC_1$  bond length was set to 0.3 nm (with a bond force

constant of  $K = 5000 \text{ kJ mol}^{-1} \text{ nm}^{-2}$ ), which closely maps the CG cyclohexane to the underlying atomistic structure. Due to the larger size of the CG particles, the CG structure represents both the boat and chair configurations. Benzene is similar (see Figure 1), but with a slightly shorter equilibrium bond length of 0.27 nm (modeled as a constraint) and a more polar particle type SC<sub>4</sub> mimicking the effect of the  $\pi$ -electrons.

**2.8.2. Ions.** The CG ions are represented by Q type particles. In the case of single atom ions (e.g., sodium, chloride) the first hydration shell is considered to be included in the CG representation. In contrast to the previous version of the model, ions are now modeled with full instead of reduced charges. The increased hydration strength of ions using the “O” level interaction acts as a short-range repulsion for positive–negative ion pairs. Increasing the charge in combination with the reduced relative dielectric screening constant counteracts this effect. Consequently, the coordination numbers for ion pairs and ion–solvent remain in reasonable agreement with atomistic data, as reported previously.<sup>23</sup> Keeping in mind the difficulty of modeling of ions already with AA force fields, the CG ion force field is only qualitatively accurate.

**2.8.3. Phospholipids.** Figure 1 shows the coarse grained representation of a DPPC lipid. In the coarse grained representation, the PC headgroup consists of two hydrophilic groups: the choline (type Q<sub>0</sub>) and the phosphate group (Q<sub>a</sub>). The former bears a positive charge, the latter a negative one. For PE lipids (phosphatidylethanolamine) the positively charged group is modeled as Q<sub>d</sub>, reflecting the hydrogen-bonding capacities of the amine moiety. Two sites of intermediate hydrophilicity (N<sub>a</sub>) are used to represent the glycerol ester moiety. Each of the lipid tails is modeled by four hydrophobic particles (C<sub>1</sub>), representing 16 methylene/methyl units. Standard bonded interactions are used. The phospholipid topology in the current study is almost the same as that used in our previous work,<sup>23</sup> but the bond length of the glycerol backbone has been decreased from the standard value of  $R_{\text{bond}} = 0.47 \text{ nm}$  to 0.37 nm to better mimic the underlying chemical structure. The shorter tail lipids DLPC (dilauroyl-PC, di-C<sub>12</sub>-PC) and DCPC (dicapryloyl-PC, di-C<sub>8</sub>-PC) are modeled by removing one and two tail beads from each tail, respectively. Oleoyl tails are represented by five particles, four of C<sub>1</sub> type and a central slightly more polar one (C<sub>3</sub>) to account for the polarizable nature of the double bond. The central triplet is biased toward an off-linear configuration via a special bond angle potential for cis-double bonds (see bonded interactions).

**2.8.4. Cholesterol.** After testing several different geometries for cholesterol, we settled on the model shown in Figure 1. Cholesterol is modeled by eight particles: six representing the sterol body and two for the short tail. This mapping allows for a predominantly planar structure, while still preserving the asymmetry between the two cholesterol faces. The sterol body is mapped on a 3:1 basis, using the special class of ring type particles. A combination of bond, angle, and dihedral potentials was used to keep the ring structure rigid. The details of the cholesterol model are presented in Table 2. Perhaps a simpler representation is possible; however, the current setup allows for stable simulations with an integration time step up to 30 fs (actual simulation time).

### 3. Results and Discussion

**3.1. Thermodynamic Properties. 3.1.1. Free Energies of Vaporization, Hydration, and Partitioning.** In order to parametrize the CG model, the free energy of hydration, the free energy of vaporization, and the partitioning free energies

**TABLE 2: Overview of the Cholesterol CG Topology<sup>a</sup>**

atoms		
#	type	
1	SP <sub>1</sub>	
2	SC <sub>1</sub>	
3	SC <sub>3</sub>	
4	SC <sub>1</sub>	
5	SC <sub>1</sub>	
6	SC <sub>1</sub>	
7	SC <sub>1</sub>	
8	C <sub>1</sub>	
bonds i j		$K_{bond}$ [kJ mol <sup>-1</sup> nm <sup>-2</sup> ]
1 2		20000
2 3		20000
2 4		20000
4 7		20000
4 6		20000
5 6		20000
6 7		20000
7 8		1250
1 3		<i>constraint</i>
1 4		<i>constraint</i>
3 4		<i>constraint</i>
3 5		<i>constraint</i>
4 5		<i>constraint</i>
5 7		<i>constraint</i>
angles i j k		$K_{angle}$ [kJ mol <sup>-1</sup> ]
4 7 8		25
impropers i j k l		$K_{improper}$ [kJ mol <sup>-1</sup> rad <sup>-2</sup> ]
1 3 5 4		100
1 3 5 7		100
1 4 5 3		100
3 5 7 4		100
4 7 5 3		100
2 1 3 4		300
2 4 3 1		300
6 4 5 7		300
6 7 5 4		300

<sup>a</sup> All intramolecular interactions are excluded. The CG site numbers are shown in Figure 1.

between water and a number of organic phases (hexadecane, chloroform, ether, and octanol) were calculated for the different CG particle types. The free energy of hydration was obtained from the partitioning of CG particles between bulk water in equilibrium with its vapor. The water phase consists of 3200 water particles, with a small fraction (around 0.01 mole fraction) of other particle types. The box geometry was chosen to contain a system with a water slab surrounded by a vacuum layer of about equal size. From the equilibrium densities of the particles in the water ( $\rho_{\text{wat}}$ ) and the vapor phase ( $\rho_{\text{vap}}$ ), the hydration free energy  $\Delta G^{\text{hydr}}$  can be directly computed from

$$\Delta G^{\text{hydr}} = kT \ln(\rho_{\text{vap}}/\rho_{\text{wat}}) \quad (6)$$

Likewise, the free energy of vaporization  $\Delta G^{\text{vap}}$  can be obtained from a simulation of the pure liquid in equilibrium with its vapor. To determine the partitioning free energies  $\Delta G^{\text{part}}$  for a CG particle type, a system containing two phases (each consisting of 3200 CG sites) was set up in which a small fraction



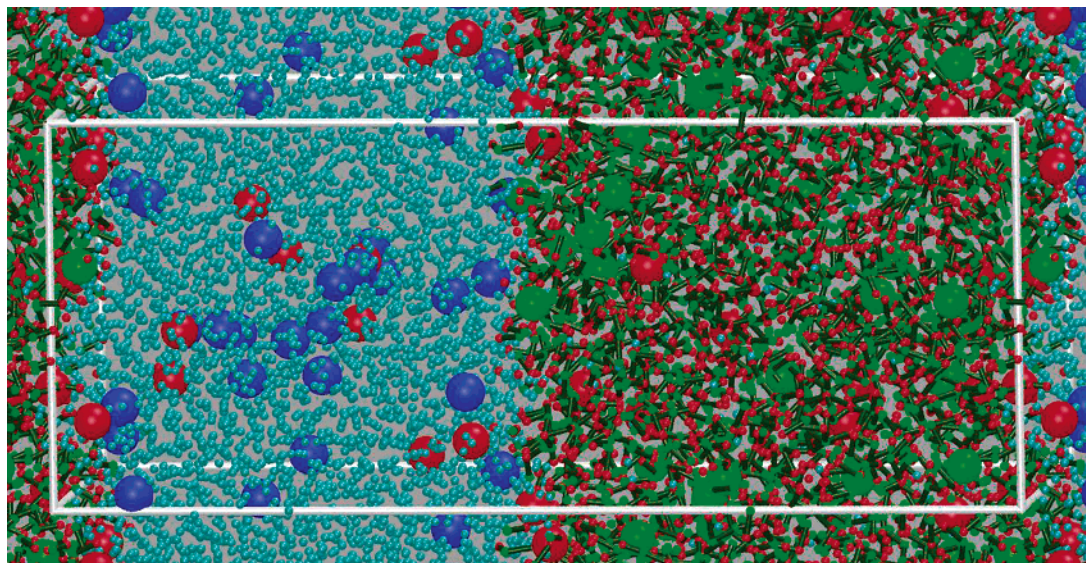


**Figure 2.** Equilibrium configuration of a water/octanol system used to determine partitioning free energies. Small beads denote the water phase ( $P_4$ ) in cyan, and the octanol phase consisting of dimers of hydrocarbon ( $C_1$ ) in green and alcohol ( $P_1$ ) in red. The larger beads represent solutes: butane ( $C_1$ ) in green, propanol ( $P_1$ ) in red, and sodium ions ( $Q_d$ ) in blue. The simulation box is indicated by thick gray lines.

(around 0.01 mole fraction) of the solvents was replaced by the CG particle under consideration. The partitioning free energy is directly obtained from the equilibrium densities of the CG particles in the water and organic solvent ( $\rho_{oil}$ ), i.e., replacing  $\rho_{vap}$  by  $\rho_{oil}$  in eq 6. With the CG model, simulations can easily be extended into the multi-microsecond range, enough to obtain statistically reliable results to within 1 kJ/mol for most particle types. All simulations were performed at  $T = 300$  K, at NVT conditions for vapor/liquid systems and at NA  $P_z$  T conditions for the liquid/liquid systems, with the normal pressure  $P_z = 1$  bar. Test simulations in which we changed the concentration of the solutes showed that a concentration of around 0.01 mol fraction is low enough to be in the regime of infinite dilution. The thickness of the solvent slabs (approximately 8 nm) is also large enough to have bulk properties in the middle of the slab, i.e., the presence of the interface is not affecting the calculated solubilities in the middle of the bulk. An example of the simulation setup is shown in Figure 2, illustrating the equilibrium distribution of a few representative CG particles between water and octanol.

In Table 3 the results of the free energy calculations are presented and compared to experimental values for representative small compounds (denoted chemical building blocks). Most selected compounds contain four heavy atoms, mimicking the basic mapping of the coarse grained model. Exceptions (i.e., building blocks containing three or five heavy atoms) are included either due to the lack of other representative compounds or for comparative reasons. Because experimental data for the partitioning of representative charged species are rare and their interpretation is problematic, these data are not included.

The CG model reproduces the correct trend for free energies of vaporization and hydration, although the actual values are systematically too high. This observation is in agreement with calculations of thermodynamic properties of alkanes and water performed by Baron et al.<sup>48</sup> From these studies it was concluded that the CG model underestimates the interaction energy between alkanes and overestimates the repulsion between water and alkanes. Compared to our previous model, the interaction between alkane sites has increased slightly (from  $\epsilon = 3.4$  to  $3.5$  kJ mol<sup>-1</sup>) and the effective repulsion between water and alkanes has been lowered (increase of  $\epsilon$  from 1.8 to 2.0 kJ mol<sup>-1</sup>). Although the vaporization free energies for the most

apolar compounds are now well approximated, the changes are still insufficient to reproduce the solvation and vaporization free energies on a quantitative level for the whole range of compounds. Increasing the interactions among the more polar CG sites is not an option, as the solid phase appears stable for  $P_5$  particles (interacting with level O) at room temperature. For  $P_4$  particles (water), the fluid phase is only marginally stable at room temperature. With respect to both the vapor and the solid phase, the CG condensed phase is therefore not as stable as it should be. This is a known consequence of using a LJ 12-6 interaction potential, which has a limited fluid range. Switching to a different nonbonded interaction potential could, in principle, improve the relative stability of the fluid phase. However, a complete reparametrization of the CG model would be required which is beyond the scope of the current work. As long as its applications are aimed at studying the condensed phase and not at reproducing gas/fluid or solid/fluid coexistence regions, the most important thermodynamic property is the partitioning free energy. Importantly, the water/oil partitioning behavior of a wide variety of compounds can be accurately reproduced with the current parametrization of the CG model. Table 3 shows results obtained for the partitioning between water and a range of organic phases of increasing polarity (hexadecane, chloroform, ether, and octanol) for each of the 18 CG particle types. Where available, comparison to experimental data reveals a close agreement to within 2 kT for almost all compounds and phases; indeed, agreement is within 1 kT for many of them. Expecting more accuracy of a CG model might be unrealistic.

**3.1.2. Interfacial Tension.** Another important thermodynamic property is the interfacial tension, a measure of the free energy cost associated with the formation of an interface between different solvents. We calculated the interfacial tension  $\gamma$  from the average perpendicular  $P_z$  and lateral  $P_{||}$  pressure components according to

$$\gamma = \frac{1}{2} L \langle P_z - P_{||} \rangle \quad (7)$$

Here  $\langle \rangle$  denotes an ensemble average and  $L$  the box length. The factor (1/2) accounts for the two interfaces present in the chosen setup. Three systems were simulated: slabs of water and dodecane in equilibrium with a vacuum slab, and a water

**TABLE 3: Thermodynamic Properties of the CG Particle Types<sup>a</sup>**

type	building block	examples	$\Delta G^{\text{vap}}$		$\Delta G^{\text{hyd}}$		$\Delta G^{\text{part}}_{\text{HW}}$		$\Delta G^{\text{part}}_{\text{CW}}$		$\Delta G^{\text{part}}_{\text{EW}}$		$\Delta G^{\text{part}}_{\text{OW}}$	
			exp	CG	exp	CG	exp	CG	exp	CG	exp	CG	exp	CG
Q <sub>da</sub>	H <sub>3</sub> N <sup>+</sup> -C <sub>2</sub> -OH	ethanolamine (protonated)			-25		< -30		-18		-13		-18	
Q <sub>d</sub>	H <sub>3</sub> N <sup>+</sup> -C <sub>3</sub>	1-propylamine (protonated)			-25		< -30		-18		-13		-18	
	NA <sup>+</sup> OH	sodium (hydrated)			-25		< -30		-18		-13		-18	
Q <sub>a</sub>	PO <sub>4</sub> <sup>-</sup>	phosphate			-25		< -30		-18		-13		-18	
	CL <sup>-</sup> HO	chloride (hydrated)			-25		< -30		-18		-13		-18	
Q <sub>0</sub>	C <sub>3</sub> N <sup>+</sup>	choline			-25		< -30		-18		-13		-18	
P <sub>5</sub>	H <sub>2</sub> N-C <sub>2</sub> =O	acetamide	sol	sol	-40	-25	-27	-28	(-20)	-18	-15	-13	-8	-10
P <sub>4</sub>	HOH (× 4)	water	-27	-18	-27	-18	-25	-23		-14	-10	-7	-8	-9
	HO-C <sub>2</sub> -OH	ethanediol	-35	-18	-33	-18	-21	-23		-14		-7	-8	-9
P <sub>3</sub>	HO-C <sub>2</sub> =O	acetic acid	-31	-18	-29	-18	-19	-21	-9	-10	-2	-6	-1	-7
	C-NH-C=O	methylformamide	-35	-18		-18		-21		-10		-6	-5	-7
P <sub>2</sub>	C <sub>2</sub> -OH	ethanol	-22	-16	-21	-14	-13	-17	-5	-2	-3	1	-2	-2
P <sub>1</sub>	C <sub>3</sub> -OH	1-propanol	-23	-16	-21	-14	-9	-11	-2	-2	0	1	1	-1
		2-propanol	-22	-16	-20	-14	-10	-11	-2	-2	-1	1	0	-1
N <sub>da</sub>	C <sub>4</sub> -OH	1-butanol	-25	-16	-20	-9	-5	-7	2	0	4	2	4	3
N <sub>d</sub>	H <sub>2</sub> N-C <sub>3</sub>	1-propylamine	-17	-13	-18	-9	(-6)	-7	(1)	0	(-3)	2	(3)	3
N <sub>a</sub>	C <sub>3</sub> =O	2-propanone	-17	-13	-16	-9	-6	-7	1	0	-1	2	-1	3
	C-NO <sub>2</sub>	nitromethane	-23	-13	-17	-9	-6	-7		0		2	-2	3
	C <sub>3</sub> =N	propionitrile	-22	-13	-17	-9	-5	-7		0		2	1	3
	C-O-C=O	methylformate	-16	-13	-12	-9	(-6)	-7	(4)	0	(-1)	2	(0)	3
	C <sub>2</sub> HC=O	propanal		-13	-15	-9	-4	-7		0	2	2	3	3
N <sub>0</sub>	C-O-C <sub>2</sub>	methoxyethane	-13	-10	(-8)	-2	(1)	-2		6	(3)	6	(3)	5
C <sub>5</sub>	C <sub>3</sub> -SH	1-propanethiol	-17	-10		1		5		10		10		6
	C-S-C <sub>2</sub>	methyl ethyl sulfide	-17	-10	-6	1	(7)	5		10		10	(9)	6
C <sub>4</sub>	C <sub>2</sub> =C <sub>2</sub>	2-butyne	-15	-10	-1	5		9		13		13	9	9
	C=C-C=C	1,3-butadiene		-10	2	5	11	9		13		13	11	9
	C-X <sub>4</sub>	chloroform	-18	-10	-4	5	(7)	9	14	13		13	11	9
C <sub>3</sub>	C <sub>2</sub> =C <sub>2</sub>	2-butene		-10		5		13		13		13	13	14
	C <sub>3</sub> -X	1-chloropropane	-16	-10	-1	5	12	13		13		13	12	14
		2-bromopropane	-16	-10	-2	5		13		13		13	12	14
C <sub>2</sub>	C <sub>3</sub>	propane	gas	-10	8	10		16		15		14	14	16
C <sub>1</sub>	C <sub>4</sub>	butane	-11 <sup>b</sup>	-10	9	14	18	18		18		14	16	17
		isopropane	gas	-10	10	14		18		18		14	16	17

<sup>a</sup> Free energies of vaporization  $\Delta G^{\text{vap}}$ , hydration  $\Delta G^{\text{hyd}}$ , and partitioning  $G^{\text{part}}$  between water (W) and organic phases (H, hexadecane; C, chloroform; E, ether; O, octanol) are compared to experimental values. The experimental vaporization free energy was calculated from the vapor pressure  $p_{\text{vap}}$ <sup>70</sup> using  $\Delta G^{\text{vap}} = k_B T \ln(p_{\text{vap}}/k_B T c_M)$ , where  $c_M$  denotes the molar concentration of the liquid. The experimental free energies of hydration and partitioning were compiled from various sources<sup>76–84</sup> based on  $\log P$  values. The temperature for the experimental data is in the range 298–300 K, except where indicated. Simulation data were obtained at 300 K. Experimental properties between parentheses are estimates obtained from comparison to similar compounds. The statistical accuracy of the free energies obtained from the simulations is  $\pm 1$  kJ mol<sup>-1</sup>. <sup>b</sup> The temperature for the experimental data is 273 K.

**TABLE 4: Interfacial Tension (mN/m) between Different Phases<sup>a</sup>**

system	small	big	experimental
water/vapor	45	30	73
dodecane/vapor	25	23	24
water/dodecane	70	50	52

<sup>a</sup> Results from simulations are obtained both in small and in big systems. Experimental data taken from refs 70 and 85. The temperature is 293 K in all cases. The error bars are smaller than 1 mN/m.

slab in equilibrium with a dodecane slab. In order to study size effects, both a small system (400 CG beads per solvent phase) and a large system (1600 beads) were simulated. Simulations of 1  $\mu$ s proved long enough to accurately calculate the interfacial tension. The results are summarized in Table 4. Finite size effects are actually important when calculating the interfacial tension. The tension is systematically smaller for the larger system size. We attribute this to the development of capillary waves which are suppressed in the small system. Additional simulations for even larger systems show no further decrease of the measured tension. Assuming that capillary waves are also present in the experimental measurements, both the dodecane/vapor and dodecane/water interfacial tension are in good agreement with the experimental data. The water/vapor tension, however, is too low. This observation fits with the inability of the CG model to correctly reproduce the hydration free energy

of water, discussed above. Because the hydration free energy is too low, the cost of creating a water/vapor interface is also too low.

**3.2. Improved Bilayer Properties.** Many properties of lipid bilayers could be reproduced on a semiquantitative level with the original version of the CG model,<sup>23</sup> including the area per headgroup for both saturated and unsaturated PC and PE lipids, the distribution of groups across the membrane, and the bending and area compression moduli (for DPPC). With the new model, these properties stay unaffected within the statistical uncertainties. In the next paragraphs we focus on a few thermodynamic properties of lipid bilayers that have not been addressed before, namely, the stress profile across the bilayer, the transformation of a lamellar structure into micelles, and the process of lipid desorption and flipping.

**3.2.1. Bilayer Stress Profile.** One particular problem with the original CG force field became apparent in a number of studies concerning the spontaneous curvature of the lipids. In the original publication of the CG force field<sup>23</sup> it was already noted that the tension required to stabilize a pore, characterized by a predominantly positive curvature, in a DPPC bilayer was too high. Simulations of mixed bicelles consisting of long-tail DPPC and short-tail DCPC lipids also revealed that the propensity of the short-tail lipids for the positively curved rim of the bicelle was too low.<sup>40</sup> In fact, systems of pure DCPC

lipids still formed bilayers, in contrast to the known experimental behavior. Furthermore, simulations of the phase transformation between the lamellar and inverted hexagonal phase of DOPC/DOPE (dioleoyl-PC/dioleoyl-PE) mixtures<sup>35</sup> showed that the inverted hexagonal phase was too stable with respect to experimental data. In both the bicelle simulations and the inverted hexagonal phase formation the behavior could be improved by increasing the hydration strength of the phosphate moieties. This redistributes the stress toward the headgroup area, increasing the spontaneous curvature. Although this ad hoc solution worked well, it is not very satisfactory. In the newly parametrized model, the headgroup is more strongly hydrated, so we expect, at least qualitatively, a similar effect.

To study the effect of the new parameters quantitatively, the stress profile  $\Sigma(z) = \langle P_z - P_{||}(z) \rangle$  across the bilayer has been computed. Although the pressure components cannot be unambiguously locally distributed, as long as short-range forces dominate, the particular local assignment procedure appears not to be very important.<sup>52</sup> From the first moment of the stress profile, the spontaneous monolayer curvature  $c_0$  can be obtained

$$c_0 = \frac{1}{k_m} \int_0^\infty z \Sigma(z) dz \quad (8)$$

Here  $k_m$  is the monolayer bending modulus ( $=k_b/2$ ), half of the bilayer bending modulus) and  $z$  the distance across the membrane relative to the center of the bilayer ( $z = 0$ ). We have to keep in mind that also this expression is not independent of the choice of definition of local pressure.<sup>53</sup> As a qualitative measure it is nevertheless useful. Increasingly positive values for the radius of spontaneous curvature reflect increased preference for positively curved surfaces (micelles, pores), increasingly negative values correspond to an increasing preference for negatively curved surfaces (inverted phases, stalks). We calculated the stress profiles for both a CG and an AA DPPC bilayer, using the method described by Lindahl et al.<sup>54</sup> For the atomic level simulation, a bilayer of 256 lipids at a limited hydration level (29 waters/lipid) was chosen to keep the computations feasible. The force field and simulation parameters were taken from a previous study (setup E,<sup>55</sup>). For the CG model the stress profiles converge much more rapidly, allowing a larger membrane patch (512 lipids) and inclusion of a bulk water layer (47 waters/lipid). Both the CG and AA systems were simulated at zero overall surface tension, at  $T = 323$  K.

In Figure 3 the resulting stress profiles for a DPPC bilayer are compared, together with results for the original CG model. Comparing the AA profile to the CG profiles reveals a close correspondence of the main features of the stress profile, especially in the newly parametrized version. The main compressive stress is present at the border between the headgroup and tail region of the bilayer, balanced by two regions of expansive stress at the headgroup/water interface and in the bilayer core. The agreement is not just on a qualitative level. Both profiles have similar amplitudes on the absolute pressure scale. Similar profiles from atomistic simulations have been obtained by others.<sup>52,54,56,57</sup> Importantly, the first moment is equal. The first moment is related to the product of the monolayer bending modulus and the spontaneous curvature (eq 8). In order to compare to experimental estimates for the spontaneous curvature, knowledge of the bending modulus is required. The bending rigidity for the CG DPPC bilayer is somewhat uncertain. Originally a value of  $k_b = 4 \times 10^{-20}$  J was obtained.<sup>23</sup> More recently, however, a value twice as large was calculated for the same system.<sup>58</sup> The latter estimate falls within the range of experimental values,  $k_b = 2k_m = (6-14) \times$

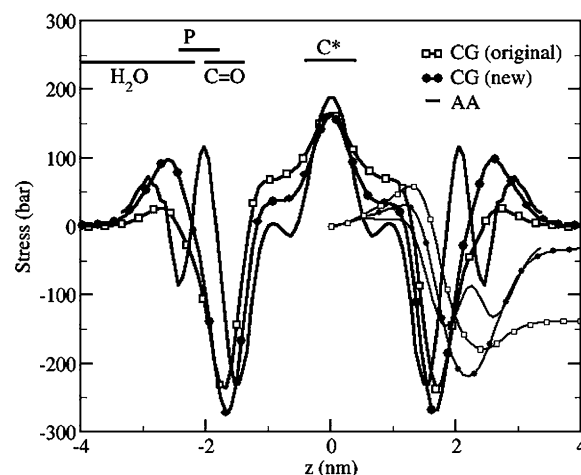


**Figure 3.** Stress profiles for a DPPC bilayer with the original and the new CG force field, compared to results obtained for a DPPC bilayer simulated at atomistic detail. Thinner lines denote the running integrand of the first moment of the stress profile across one of the monolayers. The plateau value reached in the aqueous phase is proportional to the spontaneous curvature. The mean position and width of the distribution of several key groups (water, phosphate, carbonyl and terminal methyl group) are given for reference.

**TABLE 5: Overview of the Spontaneous Curvature of Lipids Obtained from Simulations, Compared to Experimental Estimates<sup>a</sup>**

lipid	$c_0$ (nm <sup>-1</sup> )	
	simulation	experimental
DPPC	-0.02 to -0.05	~0
(original CG)	-0.1 to -0.2	
(all atom)	-0.02 to -0.05	
DOPC	-0.07 to -0.15	-0.05, -0.1
DPPE	-0.12 to -0.28	
DOPE	-0.15 to -0.35	-0.33, -0.48

<sup>a</sup> Experimental estimates for DOPC and DOPE were taken from refs 86 and 87. For DPPC, a lamellar phase preferring lipid, the precise intrinsic curvature is experimentally difficult to estimate but is approximately zero. The simulation results were obtained using eq 8. The range of values given for  $c_0$  obtained from the simulations reflects the range of bending constants  $k_b = 2k_m = (6-14) \times 10^{-20}$  J reported in the literature (e.g., refs 59-61).

$10^{-20}$  J for most phospholipids (e.g., refs 59-61). Monounsaturated lipids apparently also lie within this range.<sup>62</sup> We used the experimental range of values to extract the spontaneous curvature from eq 8. The results are presented in Table 5 for DPPC, DOPC, DOPE, and DPPE CG bilayers. Despite the uncertainties in the extraction procedure of the spontaneous curvature from the stress profiles, and the uncertainties in the stress profiles themselves, a few significant observations can be made. For DPPC, the value of the spontaneous curvature is very small, reflecting that DPPC is a cylindrically shaped lipid that prefers to stay in a lamellar phase. Increasing the unsaturation or substituting the PC headgroup for the smaller PE headgroup results in a negative spontaneous curvature, in good agreement with the experimental trend. With the previous version of the CG model, the spontaneous curvature of DPPC was four times larger than that in the newly parametrized version, clearly overestimating the propensity to form negatively curved interfaces. In conclusion, both the stress profile and the first moment have improved with respect to the original model.

**3.2.2. Lamellar-Micellar Transition.** Because the original model overestimated the negative spontaneous curvature, short-tail lipid bilayers tended to be too stable in comparison to experiment. Experimentally, stable phospholipid bilayers can



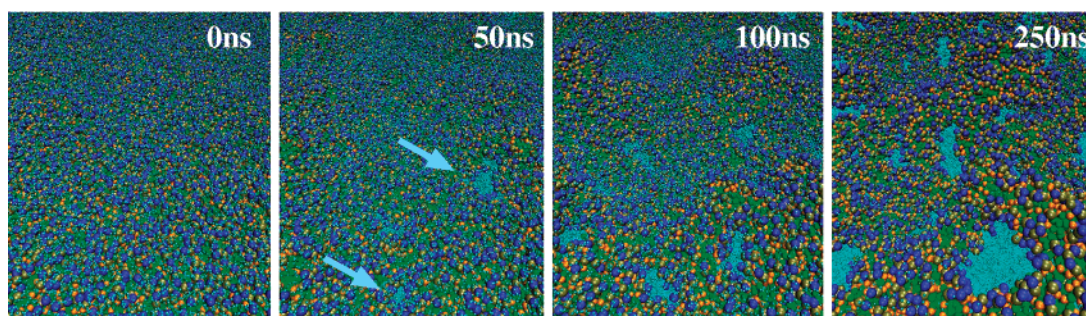


**Figure 4.** Lamellar-to-micellar transformation of a bilayer composed of short-tail lipids (DCPC). Starting from a bilayer state, pores form spontaneously after 50 ns (arrows). The pores expand irregularly, eventually transforming the bilayer into a solution of interconnected wormlike micelles.

be formed down to nine carbons per tail.<sup>63</sup> Shorter tail lipids prefer to form micelles due to their intrinsic preference for positively curved surfaces. With the original model, a DCPC bilayer (eight carbons per tail) was stable over simulation times exceeding

1  $\mu$ s and system sizes of thousands of lipids. Moreover, a random solution of DCPC lipids formed bilayers upon spontaneous aggregation, indicating that the apparent stability is of thermodynamic origin and not merely kinetic. In contrast, with the newly parametrized force field the DCPC bilayer spontaneously disintegrates, forming a micellar solution. Graphical snapshots illustrating this process for a bilayer containing 256 DCPC lipids are shown in Figure 4. The bilayer was simulated at conditions of zero surface tension at  $T = 325$  K. After a short period of metastability (50 ns), pores spontaneously form in the lipid matrix. Once formed, the pores start growing and eventually rupture the complete bilayer. Due to the high concentration of lipids, no spherical micelles are formed, but rather a connected network of wormlike micelles appears. Simulations of DLPC lipids (three CG beads per tail) spontaneously aggregating from randomized starting structures show an exclusive preference for bilayers. The line tension thus vanishes as a function of lipid tail length at about eight carbons per tail for a PC lipid simulated with the new CG model, in agreement with the experimental findings. Note the irregular shape of the pores in Figure 4, a consequence of the vanishing line tension.

### 3.2.3. Free Energy of Lipid Desorption and Flip-Flopping.

The potential of mean force (PMF) of a phospholipid in a bilayer is a key microscopic thermodynamic property that describes the energetic cost of localized lipid defects and provides a link between the critical micelle concentration and lipid aggregates. Previously we have calculated the PMF for an atomistic DPPC model,<sup>64</sup> using umbrella sampling<sup>65</sup> to both extract a lipid from the bilayer and force a lipid into the bilayer interior. Here we repeat these calculations for the new CG model, both for DPPC and for DLPC bilayers. The bilayer consists of 128 lipids and 3466 CG water particles. This system is much larger than the atomistic system because the computational cost to simulate the CG lipids is much lower. The amount of water is excessive (exceeding 100 waters/lipid) to avoid lipids interacting with the periodic bilayer image when extracted into the water phase. The temperature is set to 325 K and both lateral and perpendicular pressures to 1 bar, the same as used in the atomistic study. The umbrella potential acts on the center of mass of the phosphate group of two lipids independently, one in each leaflet, with a harmonic potential with a force constant of  $3200 \text{ kJ mol}^{-1} \text{ nm}^{-2}$ . The two lipids were offset by 4 nm, so that in the first simulation one lipid was constrained at 0 nm (corresponding to the center of the bilayer) and the second lipid at 4 nm (corresponding to bulk water outside the bilayer). In the remaining 60 simulations both lipids were shifted by 0.2 nm per simulation, corresponding

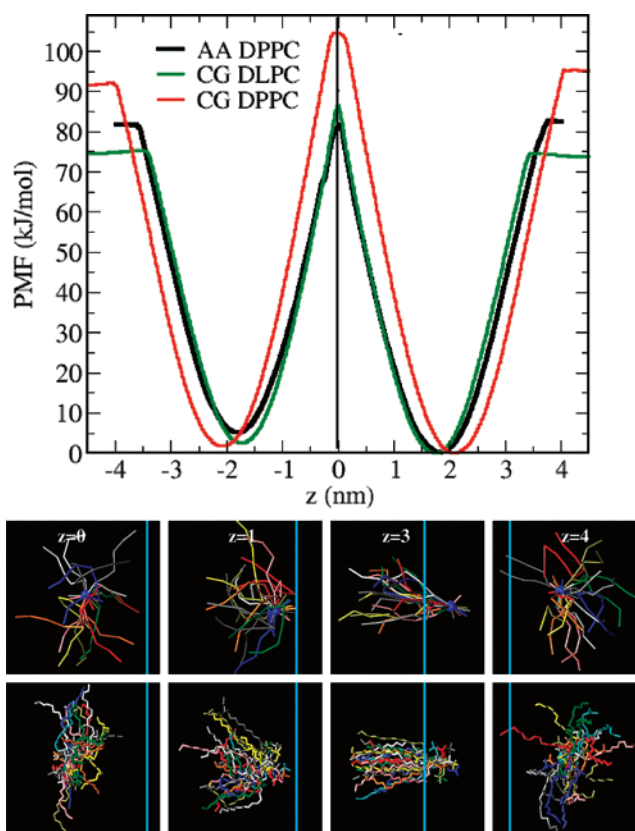


**Figure 5.** Potential of mean force of extracting a lipid from, and traversing a lipid through a bilayer. The upper graph compares results from AA simulations (DPPC) and the new CG model (DPPC and DLPC). Underneath graphical snapshots illustrate the conformational spread of the DPPC lipids (CG upper row, AA lower row) constrained at various depths along the membrane normal. The position  $z = 0$  nm corresponds to the center of the bilayer; the equilibrium position of the phosphate group is indicated by the cyan line at  $z = 2$  nm.

to 61 windows. Each window was then simulated for 4  $\mu$ s. The PMF profile was constructed from the biased distributions of the centers of mass of the lipids using the weighted histogram analysis method.<sup>66</sup> Thus we have data for two approximately independent lipids, which provides a way to estimate errors in the calculations.

Figure 5 shows the PMF for both the AA and the CG lipids and a number of snapshots that illustrate the conformational space sampled by the lipids at various depths. The general features of both the AA and the CG model appear very similar, although the exact values differ somewhat. The profiles are characterized by a deep minimum at the equilibrium position in the bilayer, steeply rising for displacements both deeper into the bilayer and moving away from the bilayer. As the lipid loses contact with the bilayer the profile abruptly flattens without a

significant barrier. The difference in the PMF near the equilibrium position of the lipid in the bilayer and in the middle of the water phase is ca. 80 kJ/mol for the atomistic DPPC. This value agrees reasonably well with the free energy difference of 69 kJ/mol estimated<sup>64</sup> from the experimentally determined critical micelle concentration ( $5 \times 10^{-10}$  M at 298 K<sup>67</sup>). The CG model for DPPC gives a slightly larger value ( $\sim 90$  kJ/mol). The slope of the PMF is, however, very similar. The difference in the total free energy cost of extracting the DPPC lipid originates from the slight difference in thickness of the bilayer which is apparent from the distance between the minima in the PMF. For the shorter DLPC membrane indeed a smaller value of  $\sim 75$  kJ/mol is computed.

When a lipid is forced inside the bilayer, significant water/lipid defects form using the atomistic representation. Near the center of the bilayer, a small water pore opens up across the membrane. This is not observed with the CG model, neither for DPPC nor for the thinner DLPC membrane, although the free energy cost of solubilizing the lipid headgroup in the bilayer interior is of similar magnitude. A possible explanation of this discrepancy touches upon a major simplification made in the CG model, namely, the assumption of a uniform dielectric constant across the entire system. In reality, mimicked in AA level simulations, polar interactions become stronger inside an apolar medium due to the lack of screening. For a lipid headgroup dragged inside the bilayer interior, this implies that the interaction with neighboring headgroups becomes stronger, thus favoring the formation of an entire headgroup-lined pore across the bilayer. For the CG model this effect is absent, although the increased repulsion between charged and apolar groups (interaction level IX) mimics part of this effect, resulting in the retainment of the hydration shell inside the bilayer. As a more fundamental solution one could think of using a position dependent dielectric screening constant. To avoid preassumptions about the state of a system, this should be done in an adaptive manner, i.e., depending on the instantaneous local environment of a particle. Alternatively, the water model could be revised to include a dipole. Investigation of these alternatives is left for future study. With the current model, caution is required when moving charged or hydrophilic compounds into a low dielectric medium. As this is an unlikely event, systems simulated close to equilibrium conditions are not expected to suffer from this problem, however. Considering the free energy profiles in Figure 5, even perturbations of the equilibrium position of a lipid up to 40 kJ mol<sup>-1</sup> are still accurately modeled with the CG force field.

**3.3. Extension to Ringlike Compounds. 3.3.1. Cyclohexane and Benzene.** The performance of the new class of ring-type particles in the CG model was tested on cyclohexane and benzene. Simulations were performed for systems containing 400 CG water molecules and 400 cyclohexane or benzene molecules, at a temperature  $T = 293$  K. Starting from randomly mixed conditions, the oily and aqueous phases rapidly demix into two slabs similar to the geometry depicted in Figure 2 for the octanol/water system. From the relative partitioning of water and the ring compounds between the two phases, the partitioning free energy of benzene in water was found to be  $22 \pm 1$  kJ mol<sup>-1</sup>, in reasonable agreement with the experimental value (16 kJ mol<sup>-1</sup><sup>68</sup>). The partitioning free energy of water into benzene,  $20 \pm 1$  kJ mol<sup>-1</sup>, is close to the experimental value (18 kJ mol<sup>-1</sup><sup>69</sup>). During a 1  $\mu$ s simulation cyclohexane was not observed to dissolve into the aqueous phase at all, and water into cyclohexane only to a very low extent ( $\sim 25$  kJ mol<sup>-1</sup>). Given the low experimental mutual solubilities of water and

saturated alkanes (no data were found for cyclohexane in particular), this appears reasonable.

Matching of the densities of the bulk fluids is less accurate. The equilibrium density of cyclohexane in the middle of the cyclohexane slab is 0.72 g cm<sup>-3</sup> (experimental density 0.78 g cm<sup>-3</sup> at 293 K<sup>70</sup>). For CG benzene we find the same density, whereas the experimental density is much higher (0.87 g cm<sup>-3</sup> at 293 K<sup>70</sup>). Various approaches have been used to increase the density of the small ring compounds, including the use of smaller beads, shorter bonds or stronger ring–ring interactions. However, these attempts resulted either in solid phases or in solubility data that got much worse. Because we consider the proper partitioning behavior of the compounds most important, we settled for the model described above. For applications in which the behavior of ring–ring interactions play an important role, some caution is advised.

**3.3.2. Cholesterol.** In order to test the cholesterol model in a lipid membrane environment, we focus here on the well-known condensing effect of cholesterol on the area per lipid. This condensation effect has been observed experimentally (for a recent review see ref 71) and also in many atomic level simulations (e.g., refs 72–74). The condensation effect is caused by an increase in lipid tail order of lipids surrounding cholesterol.

Simulations of mixed cholesterol/DPPC systems were set up, covering a range of cholesterol mole fractions, from 0 up to 0.6. Each of the systems consists of a total of 256 lipid molecules, solvated by 32 waters/lipid (8 CG waters/lipid). The simulations cover multiple microseconds and were performed at  $T = 323$  K under zero surface tension conditions. Figure 6 shows a snapshot of the system with a cholesterol mole fraction of 0.3. The cholesterol is oriented perpendicular to the membrane surface, with the polar site representing the hydroxyl group residing at the level of the DPPC glycerol moieties and the tail residing near the center of the bilayer interior. The location of cholesterol with respect to the other membrane components is very similar to that observed in atomic level simulations.<sup>72–74</sup> The expected increased ordering of the lipid tails at this relatively high cholesterol concentration is noticeable. Analysis of the lateral diffusion rates of the components (not shown) reveals that the bilayer is still in the (ordered) fluid phase. To quantify the condensing effect, in Figure 7 the area per lipid is shown as a function of the cholesterol mole fraction. For comparison, results from the atomic level study of Hofsäuss et al.<sup>74</sup> and a prediction (also based on atomic level simulations) from Edholm and Nagle<sup>75</sup> are included as well. The level of agreement between the CG data and the atomistic data is very satisfactory, especially for a cholesterol mole fraction larger than 0.15. A more elaborate investigation of the properties of CG DPPC/cholesterol bilayers is currently underway.

**3.4. Coarse Graining Recipe.** Finally we present a simple three-step recipe, or guide, on how to proceed in parametrizing new molecules using the CG model. The first step consists of mapping the chemical structure to the CG representation, the second step is the selection of appropriate bonded interactions, and the third step is the optimization of the model by comparing to AA level simulations and/or experimental data. A few limitations about the application are also given.

**Step I, Mapping onto CG Representation.** The first step consists of dividing the molecule into small chemical building blocks, ideally of four heavy atoms each. The mapping of CG particle types to chemical building blocks, as presented in Table 3, subsequently serves as a guide toward the assignment of CG particle types. Because most molecules cannot be entirely



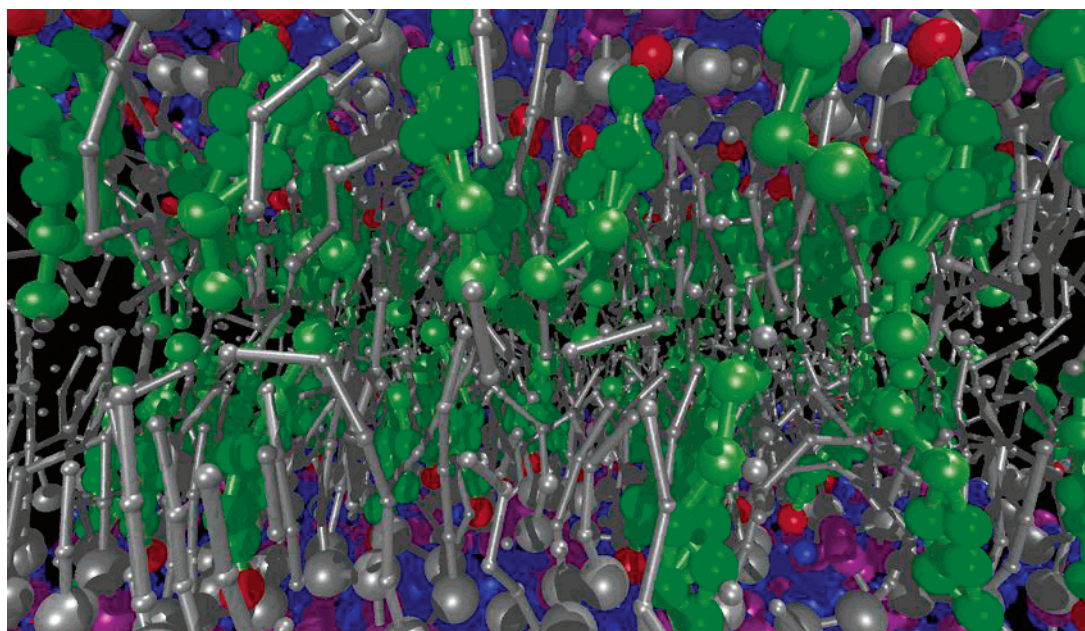


**Figure 6.** Structure of a DPPC/cholesterol bilayer at 0.3 mole fraction cholesterol after 1  $\mu$ s simulation with the new CG model. Cholesterol molecules are displayed in green, with a lighter shade for the two tail beads. The cholesterol site representing the hydroxyl group is shown in red. The DPPC lipid tails are shown in silver, with larger spheres denoting the glycerol moiety. Lipid headgroups are displayed in purple (phosphate) and blue (choline).

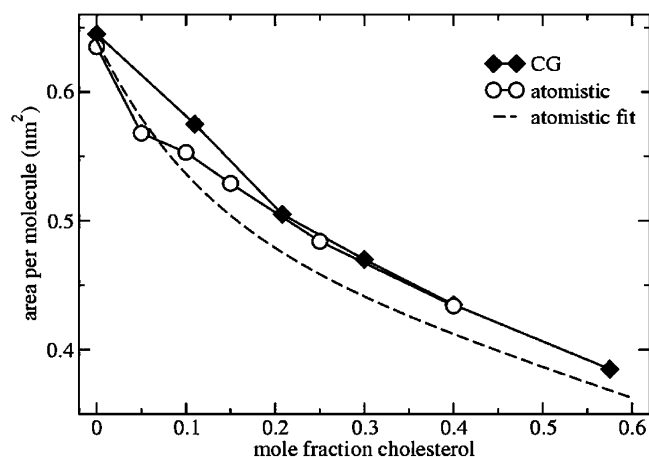


**Figure 7.** Condensating effect of cholesterol on membrane area. The new CG model is compared to atomistic data from Hofsäss et al.<sup>74</sup> and to a fit of multiple atomistic data sets as presented by Edholm and Nagle.<sup>75</sup> All simulations were performed at  $T = 323$  K.

mapped onto groups of four heavy atoms, however, some groups will represent a smaller or larger number of atoms. In fact there is no reason to map on to an integer number of atoms, e.g., a pentadecane mapped onto four  $C_1$  particles implies that each CG bead represents  $3^{3/4}$  methyl(ene) groups. In the case of more substantial deviations from the standard mapping scheme, small adjustments can be made to the standard assignment. For instance, a group of three methyl(ene)s is more accurately modeled by a  $C_2$  particle (propane) than the standard  $C_1$  particle for saturated alkanes. The same effect is illustrated by the alcohols: whereas the standard alcohol group is modeled by a  $P_1$  particle (propanol), a group representing one less carbon is more polar ( $P_2$ , ethanol) whereas adding a carbon has the opposite effect ( $N_{da}$ , butanol). Similar strategies can be used for modulation of other building blocks. To model compounds containing rings, a more fine grained mapping procedure can be used. In those cases, the special class of S-particles is appropriate.

**Step II, Selecting Bonded Interactions.** For most molecules the use of a standard bond length (0.47 nm) and force constant of  $K_{\text{bond}} = 1250 \text{ kJ mol}^{-1} \text{ nm}^{-2}$  seems to work well. In cases where the underlying chemical structure is better represented using different values, however, there is no restriction in adjusting these values. Especially for ring structures much smaller bond lengths are required. For rigid rings, the harmonic bond and angle potentials are better replaced by a constraint, as was done for benzene and cholesterol. For linear chainlike molecules, a standard force constant of  $K_{\text{angle}} = 25 \text{ kJ mol}^{-1}$  with an equilibrium bond angle  $\theta_0 = 180^\circ$  is the best initial choice. The angle may be set to smaller values to model unsaturated cis-bonds, or to mimic the underlying equilibrium structure more closely in general. In order to keep ring structures planar, dihedral angles should be added. For more complex molecules (e.g., cholesterol) multiple ways exist for defining the bonded interactions. Not all of the possible ways are likely to be stable with the preferred time step of 30–40 fs. Some trial-and-error testing is required to select the optimal set.

**Step III, Optimization.** The coarse graining procedure does not have to lead to a unique assignment of particle types and bonded interactions. A powerful way to improve the model is by comparison to AA level simulations, analogous to the use of quantum calculations to improve atomistic models. Structural comparison is especially useful for optimization of the bonded interactions. For instance, the angle distribution function for a CG triplet can be directly compared to the distribution function obtained from the AA simulation of the centers of mass of the corresponding atoms. The optimal value for the equilibrium angle and force constant can thus be extracted. Comparison of thermodynamic behavior is a crucial test for the assignment of particle types. Both AA level simulations (e.g., preferred position of a probe inside a membrane) and experimental data (e.g., the partitioning free energy of the molecule between different phases) are useful for a good assessment of the quality of the model. The balance of forces determining the partitioning behavior can be very subtle. A slightly alternative assignment of particle types may significantly improve the model. Once



more, it is important to stress that Table 3 serves as a guide only; ultimately the comparison to AA simulations and experimental data should be the deciding factor in choosing parameters.

**Limitations.** The potential range of applications of the CG model is very broad. There are however certain important limitations which should be kept in mind. First of all, the model has been parametrized for the fluid phase. Properties of solids, such as crystal packing, are not expected to be accurate. Both the gas and the solid phase appear somewhat too stable with respect to the fluid phase. The thermodynamic behavior of solid/fluid and gas/fluid interfaces is therefore also problematic, at least at the quantitative level. In applications where such interfaces are formed (especially the water/vapor interface in, e.g., rupture of lipid monolayers<sup>42</sup>) these limitations have to be kept in mind.

Furthermore, the parametrization is based on free energies. The inherent entropy loss on coarse graining is necessarily compensated for by a reduced enthalpy term.<sup>48</sup> The enthalpy/entropy compensation observed in many processes is therefore not as large when modeled at the CG level. Consequently, also the temperature dependence is affected, although not necessarily weaker. For instance, the temperature-dependent hydration free energy for linear alkanes was found to be more pronounced in the CG representation compared to a AA representation.<sup>48</sup> Similar to any force field, applications outside the temperature range used for parametrization (~270–330 K) have to be considered with care. Another difficulty encountered in our CG model, and perhaps in most CGing approaches, is to model the partitioning of polar and charged compounds into a low dielectric medium. Because of the implicit screening, the interaction strength of polar substances is underestimated in nonpolarizable solvents. Applications involving the formation of polar/charged complexes in a nonpolar environment are especially prone to be affected. The inability to form a transmembrane water pore upon dragging a lipid across the membrane is an example. Besides the implicit screening in the CG model, the neglect of long-range electrostatic forces poses a further limitation. Pairwise interactions beyond 1.2 nm (between two and three CG beads away) are not taken into account. In principle long-range electrostatic interactions could be added to the CG model, in similar ways as it is done in atomistic simulations. This approach was in fact taken in a few applications with the previous version of our CG model.<sup>41,45</sup> One has to realize that a modification of the electrostatic interaction scheme may affect other properties such as the area per lipid or the spontaneous curvature.

#### 4. Conclusion

In this paper a new version of the CG lipid and surfactant model<sup>23</sup> has been presented, coined the MARTINI force field for biomolecular simulations. The key feature of the model is its systematic parametrization based on thermodynamic data, especially experimental partitioning data. Since most applications of the CG model are naturally in the condensed phase, the reproduction of the experimental partitioning free energies is essential. We have shown that the newly parametrized model leads to improved behavior of lipid bilayers in terms of the stress profile across the bilayer and its tendency to form pores. Accurate agreement with all atom simulations is further shown for the free energy of lipid desorption and, to a lesser extent, flip-flopping across the bilayer. With the ultimate aim of extending the CG model to model all biomolecules, a special class of particles has been introduced for rings. As a first

application, cholesterol was modeled. The well-known condensing effect of cholesterol on the area per lipid could be quantitatively reproduced. Currently parametrization of all amino acids is underway, based on the model presented in this paper.

**Acknowledgment.** S.J.M. acknowledges financial support from The Netherlands Organisation for Scientific Research (NWO). D.P.T. is an AHFMR Senior Scholar and CIHR New Investigator. D.P.T. is supported by NSERC. The help of Marlon Hinner and Cesar Lopez Bautista is greatly appreciated.

#### References and Notes

- (1) Smit, B.; Hilbers, P. A. J.; Esselink, K.; Rupert, L. A. M.; van Os, N. M.; Schlijper, A. G. *Nature* **1990**, *348*, 624–625.
- (2) Shillcock, J. C.; Lipowsky, R. *J. Phys.: Condens. Matter* **2006**, *18*, S1191–S1219.
- (3) Venturoli, M.; Sperotto, M. M.; Kranenburg, M.; Smit, B. *Phys. Lett.* **2006**, *437*, 1–54.
- (4) Müller, M.; Katsov, K.; Schick, M. *Phys. Lett.* **2006**, *434*, 113–176.
- (5) Noguchi, H.; Takasu, M. *Phys. Rev. E* **2001**, *64*, 41913.
- (6) Farago, O. *J. Chem. Phys.* **2003**, *119*, 596–605.
- (7) Müller, M.; Katsov, K.; Schick, M. *Biophys. J.* **2003**, *85*, 1611–1623.
- (8) Brannigan, G.; Brown, F. L. H. *J. Chem. Phys.* **2004**, *120*, 1059–1071.
- (9) Murtola, T.; Falck, E.; Patra, M.; Karttunen, M.; Vattulainen, I. *J. Chem. Phys.* **2004**, *121*, 9156–9165.
- (10) Sevink, G. J. A.; Zvelindovsky, A. V. *Macromolecules* **2005**, *38*, 7502.
- (11) Cooke, I. R.; Kremer, K.; Deserno, M. *Phys. Rev. E* **2005**, *72*, 011506.
- (12) Wang, Z.; Frenkel, D. *J. Chem. Phys.* **2005**, *122*, 234711.
- (13) Goetz, R.; Lipowsky, R. *J. Chem. Phys.* **1998**, *108*, 7397–7409.
- (14) Venturoli, M.; Smit, B. *Phys. Chem. Commun.* **1999**, *10*, 1–5.
- (15) Groot, R. D.; Rabone, K. L. *Biophys. J.* **2001**, *81*, 725–736.
- (16) Shillcock, J. C.; Lipowsky, R. *J. Chem. Phys.* **2002**, *117*, 5048–5061.
- (17) den Otter, W. K.; Briels, W. J. *J. Chem. Phys.* **2003**, *118*, 4712–4720.
- (18) Stevens, M. J. *J. Chem. Phys.* **2004**, *121*, 11942–11948.
- (19) Frink, L. J. D.; Frischknecht, A. L. *Phys. Rev. E* **2005**, *72*, 041923.
- (20) Markvoort, A. J.; Pieterse, K.; Steijaert, M. N.; Spijker, P.; Hilbers, P. A. J. *J. Phys. Chem. B* **2005**, *109*, 22649–22654.
- (21) Pool, R.; Bolhuis, P. G. *Phys. Chem. Chem. Phys.* **2006**, *8*, 941–948.
- (22) Shelley, J. C.; Shelley, M.; Reeder, R.; Bandyopadhyay, S.; Klein, M. L. *J. Phys. Chem. B* **2001**, *105*, 4464–4470.
- (23) Marrink, S. J.; de Vries, A. H.; Mark, A. E. *J. Phys. Chem. B* **2004**, *108*, 750–760.
- (24) Izvekov, S.; Voth, G. A. *J. Phys. Chem. B* **2005**, *109*, 2469–2473.
- (25) Lyubartsev, A. P. *Eur. Biophys. J. Biophys. Lett.* **2005**, *35*, 53–61.
- (26) Elezgaray, J.; Laguerre, M. *Comput. Phys. Commun.* **2006**, *175*, 264–268.
- (27) Oostenbrink, C.; Villa, A.; Mark, A. E.; van Gunsteren, W. F. *J. Comput. Chem.* **2004**, *25*, 1656–1676.
- (28) McWhirter, J. L. L.; Aytton, G.; Voth, G. A. *Biophys. J.* **2004**, *87*, 3242–3263.
- (29) Neri, M.; Anselmi, C.; Carnevale, V.; Vargiu, A. V.; Carloni, P. *J. Phys.: Condens. Matter* **2006**, *18*, S347–S355.
- (30) Christen, M.; van Gunsteren, W. F. *J. Chem. Phys.* **2006**, *124*, 154106.
- (31) Praprotnik, M.; Site, L. D.; Kremer, K. *J. Chem. Phys.* **2005**, *123*, 224106.
- (32) Marrink, S. J.; Mark, A. E. *J. Am. Chem. Soc.* **2003**, *125*, 15233–15242.
- (33) Marrink, S. J.; Mark, A. E. *J. Am. Chem. Soc.* **2003**, *125*, 11144–11145.
- (34) Kasson, P. M.; Kelley, N. W.; Singhal, N.; Vrljic, M.; Brunger, A. T.; Pande, V. S. *Proc. Natl. Acad. Sci. U.S.A.* **2006**, *103*, 11916–11921.
- (35) Marrink, S. J.; Mark, A. E. *Biophys. J.* **2004**, *87*, 3894–3900.
- (36) Faller, R.; Marrink, S. J. *Langmuir* **2004**, *20*, 7686–7693.
- (37) Marrink, S. J.; Risselada, J.; Mark, A. E. *Chem. Phys. Lipids* **2005**, *135*, 223–244.
- (38) Bond, P. J.; Sansom, M. S. P. *J. Am. Chem. Soc.* **2006**, *128*, 2697–2704.
- (39) Shih, A. Y.; Arkhipov, A.; Freddolino, P. L.; Schulten, K. *J. Phys. Chem. B* **2006**, *110*, 3674–3684.

- (40) de Joannis, J.; Jiang, F. Y.; Kindt, J. T. *Langmuir* **2006**, *22*, 998–1005.
- (41) Adhangale, P. S.; Gaver, D. P. *Mol. Phys.* **2006**, *104*, 3011–3019.
- (42) Baoukina, S.; Monticelli, L.; Marrink, S. J.; Tieleman, D. P. Submitted for publication in *J. Am. Chem. Soc.*
- (43) Dickey, A. N.; Faller, R. J. *Polym. Sci.* **2005**, *43*, 1025–1032.
- (44) R. Notman, M. Noro, B. O.; Anwar, J. *J. Am. Chem. Soc.* **2006**, *128*, 13982–13983.
- (45) Lee, H.; Larson, R. G. *J. Phys. Chem. B* **2006**, *110*, 18204–18211.
- (46) Baron, R.; de Vries, A. H.; Hunenberger, P. H.; van Gunsteren, W. F. *J. Phys. Chem. B* **2006**, *110*, 8464–8473.
- (47) Baron, R.; de Vries, A. H.; Hunenberger, P. H.; van Gunsteren, W. F. *J. Phys. Chem. B* **2006**, *110*, 15602–15614.
- (48) Baron, R.; Trzesniak, D.; de Vries, A. H.; Elsener, A.; Marrink, S. J.; van Gunsteren, W. F. *Chem. Phys. Chem.* **2007**, *8*, 452–461.
- (49) Humphrey, W.; Dalke, A.; Schulten, K. *J. Mol. Graphics* **1996**, *14*, 33–38.
- (50) Lindahl, E.; Hess, B.; van der Spoel, D. *J. Mol. Model.* **2001**, *7*, 306–317.
- (51) van der Spoel, D.; Lindahl, E.; Hess, B.; Groenhof, G.; Mark, A. E.; Berendsen, H. J. C. *J. Comput. Chem.* **2005**, *26*, 1701–1718.
- (52) Sonne, J.; Hansen, F. Y.; Peters, G. H. *J. Chem. Phys.* **2005**, *122*, 124903.
- (53) Oversteegen, S. M.; Leermakers, F. A. M. *Phys. Rev. E* **2000**, *62*, 8453–8461.
- (54) Lindahl, E.; Edholm, O. *J. Chem. Phys.* **2000**, *113*, 3882–3893.
- (55) Anézo, C.; de Vries, A. H.; Höltje, H. D.; Tieleman, D. P.; Marrink, S. J. *J. Phys. Chem. B* **2003**, *107*, 9424–9433.
- (56) Gullingsrud, J.; Schulten, K. *Biophys. J.* **2005**, *86*, 3496–3509.
- (57) Patra, M. *Eur. Biophys. J. Biophys. Lett.* **2005**, *35*, 79–88.
- (58) Shkulipa, S. Computer Simulations of Lipid Bilayer Dynamics. Ph.D. thesis, University of Twente, The Netherlands, 2006.
- (59) Petrache, H. I.; Gouliava, N.; Tristram-Nagle, S.; Zhang, R. T.; Suter, R. M.; Nagle, J. F. *Phys. Rev. E* **1998**, *57*, 7014–7024.
- (60) Lee, C. H.; Lin, W. C.; Wang, J. *Phys. Rev. E* **2001**, *64*, 020901.
- (61) Shearman, G. C.; Ces, O.; Templer, R. H.; Seddon, J. M. *J. Phys.: Condens. Matter* **2006**, *18*, S1105–S1124.
- (62) Rawicz, W.; Olbrich, K. C.; McIntosh, T.; Needham, D.; Evans, E. *Biophys. J.* **2000**, *79*, 328–339.
- (63) Tausk, R. J. M.; Oudshoorn, C.; Overbeek, J. T. G. *Biophys. Chem.* **1974**, *2*, 53–63.
- (64) Tieleman, D. P.; Marrink, S. J. *J. Am. Chem. Soc.* **2006**, *128*, 12462–12467.
- (65) Torrie, G. M.; Valleau, J. J. *Comput. Phys.* **1977**, *23*, 187–199.
- (66) Kumar, S.; Bouzida, D.; Swendsen, R. H.; Kollman, P. A.; Rosenberg, J. M. *J. Comput. Chem.* **1992**, *13*, 1011–1021.
- (67) Israelachvili, J. N. *Intermolecular and surface forces*; Wiley: New York, 1992.
- (68) Schwarzenbach, R. P.; Gschwend, P. M.; Imboden, D. M. *Environmental Organic Chemistry*; John Wiley & Sons Inc.: New York, 2003.
- (69) Karlsson, R. *J. Chem. Eng. Data* **1973**, *18*, 290–292.
- (70) Lide, D. R. *CRC Handbook of Chemistry and Physics*, 72 ed.; CRC Press, Inc.: Boca Raton, FL, 1992.
- (71) McMullen, T. P. W.; Lewis, R. N. A. H.; McElhaney, R. N. *Curr. Opin. Colloid Interface Sci.* **2004**, *8*, 459–468.
- (72) Smondyrev, A.; Berkowitz, M. *Biophys. J.* **1999**, *77*, 2075–2089.
- (73) Chiu, S. W.; Jakobsson, E.; Mashl, R. J.; Scott, H. L. *Biophys. J.* **2002**, *83*, 1842–1853.
- (74) Hofsäuss, C.; Lindahl, E.; Edholm, O. *Biophys. J.* **2003**, *84*, 2192–2206.
- (75) Edholm, O.; Nagle, J. F. *Biophys. J.* **2005**, *89*, 1827–1832.
- (76) Duffy, E. M.; Jorgensen, W. L. *J. Am. Chem. Soc.* **2000**, *122*, 2878–2888.
- (77) S. Cabani, P. Gianni, V. M.; Lepori, L. *J. Solution Chem.* **1981**, *10*, 563–595.
- (78) Wolfenden, R.; Andersson, L.; Cullis, P. M.; Southgate, C. C. B. *Biochemistry* **1981**, *20*, 849–855.
- (79) Ruelle, P. *Chemosphere* **1999**, *40*, 457–512.
- (80) Dolney, D. M.; Hawkins, G. D.; Winget, P.; Liotard, D. A.; Cramer, C. J.; Truhlar, D. G. *J. Comput. Chem.* **2000**, *21*, 340–366.
- (81) Li, J.; Zhu, T.; Hawkins, G. D.; Winget, P.; Liotard, D. A.; Cramer, C. J.; Truhlar, D. G. *Theor. Chim. Acta* **1999**, *103*, 9–63.
- (82) Abraham, M. H.; Whiting, G. S.; Fuchs, R.; Chambers, E. J. *J. Chem. Soc., Perkin Trans.* **1990**, *2*, 291–300.
- (83) Viswanadhan, V. N.; Ghose, A. K.; Singh, U. C.; Wendoloski, J. J. *J. Chem. Inf. Comput. Sci.* **1999**, *39*, 405–412.
- (84) Hansch, C.; Leo, A.; Hoekman, D. *Exploring QSAR - Hydrophobic, Electronic, and Steric Constants*; American Chemical Society: Washington DC, 1995.
- (85) Amaya, J.; Rana, D.; Hornof, V. J. *Solution Chem.* **2002**, *31*, 139–148.
- (86) Hamai, C.; Yang, T.; Kataoka, S.; Cremer, P. S.; Musser, S. M. *Biophys. J.* **2006**, *90*, 1241–1248.
- (87) Zimmerberg, J.; Kozlov, M. M. *Nat. Rev. Mol. Cell Biol.* **2006**, *7*, 9–19.